Accepted Manuscript

High performance supercapacitor and non-enzymatic hydrogen peroxide sensor based on tellurium nanoparticles

M. Manikandan, S. Dhanuskodi, N. Maheshwari, G. Muralidharan, C. Revathi, R.T. Rajendra Kumar, G. Mohan Rao

PII: S2214-1804(16)30136-2
DOI: doi: 10.1016/j.sbsr.2017.02.001
Reference: SBSR 183

To appear in: *Sensing and Bio-Sensing Research*

Received date: 21 September 2016
Revised date: 23 January 2017
Accepted date: 2 February 2017

Please cite this article as: M. Manikandan, S. Dhanuskodi, N. Maheshwari, G. Muralidharan, C. Revathi, R.T. Rajendra Kumar, G. Mohan Rao , High performance supercapacitor and non-enzymatic hydrogen peroxide sensor based on tellurium nanoparticles. The address for the corresponding author was captured as affiliation for all authors. Please check if appropriate. Sbsr(2017), doi: 10.1016/j.sbsr.2017.02.001

High Performance Supercapacitor and Non-enzymatic Hydrogen Peroxide Sensor Based on Tellurium Nanoparticles

M. Manikandan[a], S. Dhanuskodi[a]*, N. Maheshwari[b], G. Muralidharan[b], C. Revathi[c], R. T. Rajendra Kumar[c] and G. Mohan Rao[d]

[a]*School of Physics, Bharathidasan University, Tiruchirappalli-620 024, India.*
[b]*Department of Physics, Gandhigram Rural Institute – Deemed University, Dindigul-624 302, India.*
[c] *Department of Nanoscience and Nanotechnology, Bharathiar University, Coimbatore-641 046, India.*
[d] *Department of Instrumentation and Applied Physics Indian Institute of Science, Bangalore-560 012, India.*
**E-mail id: dhanus2k3@yahoo.com*

Abstract

Tellurium nanoparticles (Te Nps) were synthesized by wet chemical method and characterized by XRD, Raman, FESEM, TEM, XPS, UV-Vis and FL. The Nps were coated on graphite foil and Glassy carbon electrode to prepare the electrodes for supercapacitor and biosensor applications. The supercapacitor performance is evaluated in 2 M KOH electrolyte by both Cyclic Voltammetry (CV) and galvanostatic charge-discharge method. From charge-discharge method, Te Nps show a specific capacitance of 586 F/g at 2 mA/cm^2 and 100 F/g at 30 mA/cm^2 as well as an excellent cycle life (100% after 1000 cycles). In addition, the H_2O_2 sensor performance of Te Nps modified glassy carbon electrode is checked by CV and Chronoamperometry (CA) in phosphate buffer solution (PBS). In the linear range of 0.67 to 8.04 µM of hydrogen peroxide (H_2O_2), Te NPs show a high sensitivity of 0.83 mA mM^{-1} cm^{-2} with a correlation coefficient of 0.995. The detection limit is 0.3 µM with a response time less than 5s.

Keywords: Tellurium nanoparticles, Supercapacitor, Biosensor, Hydrogen peroxide.

1. Introduction

Recently, Tellurium (Te) and Te based compounds have attracted great interest due to their outstanding physical and chemical properties. Elemental Te has been widely studied owing to its thermoelectric, nonlinear optical, gas sensing and electrochemical properties. Trigonal Te is a p-type semiconductor of bandgap 0.35 eV with a unique helical-chain conformation in its crystal structure. Thermoelectric properties of Te nanowires hybridized with carbon nanotubes show excellent mechanical stability and an electrical conductivity of 50 Sm^{-1} [1]. Nonlinear

optical transmission of Te nanowires at 532 nm exhibits excited state absorption (β $3.8x10^{-11}$ m/W) [2]. NH_3 sensing of Te nanowires by hydrazine hydrate assisted hydrothermal route displays high sensitivity, excellent selectivity, short response (5 s) and recovery (720 s) times at room temperature [3]. Similarly, electrochemistry of Te has been investigated both in acidic and alkaline media. The electrochemical behavior of Te on stainless steel substrate in alkaline solution exhibits two cathodic and an anodic peak assigned to the four electron reduction process of Te (IV) to Te (0), Te (0) to (Te-II) and the oxidation of bulk Te [4]. In the cyclic voltammetric (CV) study in HNO_3 solution (pH 2.0 and 2.5), an oxidation potential of 0.48 V is found in the forward scan. Also, with normal hydrogen electrode (NHE), the reduction potential is -0.8 V [5]. The systematic study of current-voltage measurements leads to the fabrication of electrochemical capacitors, also referred to as supercapacitors. Due to its higher charge storage and charge delivery response in comparison with other energy storage devices, supercapacitors achieved importance in modern science and technology.

The electrochemical capacitors have a large specific capacitance associated with fast charge-discharge characteristics, capable of delivering high power and exhibit a longer life cycle compared to batteries. They are mainly used in mobile phone, computer, digital camera and solar cell. In general, supercapacitor electrode materials are divided into carbon based materials, metal oxides/hydroxides and conducting polymers. Among these, carbon based materials such as activated carbon and carbon nanotubes have been used as an electrode in electric double layer capacitor (EDLC). Transition metal oxides exhibit pseudo capacitance behavior and RuO_2 has the most promising performance (953 F/g) [6]. However, the high cost, rareness and toxicity of RuO_2 have limited its commercial attractiveness. Metal tellurides also find applications in energy conversion and thermoelectric materials. Liu et al. [7] have synthesized Te/C nanocomposite in lithium –tellurium batteries with 87% storage capacity. Te/Au/MnO_2 core shell on carbon fiber as super capacitor electrode is reported with maximum specific capacitance of 930 F/g with an excellent rate capability and long cycle life (97%) [8]. Electrochemical synthesis of tellurium nanowires with a specific capacitance of 25 F/g with 46% of retention has been investigated by Tsai et al. [9].

Hydrogen peroxide (H_2O_2) finds various industrial applications such as pharmaceutical, clinical and environmental. It is a byproduct of almost all oxidases in mitochondria and separates out freely through membranes and reaches various cellular compartments. It takes part in biological functions as it is a highly reactive ion and reacts with other molecules to achieve stability. The deficiency of H_2O_2 leads to the diseases like Alzheimer's and Atherosclerosis diseases [10, 11]. Many analytical tools such as spectrophotometric, fluorometric, chemiluminescent electrochemical and volumetric have been employed for the detection of H_2O_2. It is reported that the electrochemical method owing to a low cost, highly selective, sensitive with limit of detection, wide linear range, fast response and repetitive ability plays a crucial role in the amperometric determination [12, 13]. In the last decade, the response to H_2O_2 by electrochemical biosensor modified with several metal nanomaterials has been studied [14]. Detection of H_2O_2 has been reported for Pt-TeO_2 nanowires and Pt-Te microtubes with a sensitivity of 130.6 μA mM^{-1} cm^{-2} and 2 mA mM^{-1} cm^{-2} [15, 16]. Pt-Te microtubes have also been tested against glucose and the proposed electrode shows very strong and sensitive amperometric response [17]. An electrochemical detection system based on tellurium nanowire coated glassy carbon electrodes (GCE) has been proposed by Tsai et al. to sense dopamine at nanomolar concentrations [18]. Pt nanowires core with carbon shell using Te nanowires as template has prepared by Fang et al. shows a high sensitive, wide linear range and low detection limit [10].

Tellurium nanostructures have been synthesized by different methods like hydrothermal [19], microwave assisted [20], chemical vapor deposition [8] and biomolecule assisted method [21]. Additionally, Te can react with other transition elements to generate many functional compounds such as CdTe, ZnTe, Sb_2Te_3, and PbTe. Single crystalline ZnTe nanorods have been fabricated by Hou et al. with a high blue fluorescence [22]. The effect of size and doping concentration on the power factor of n-PbTe nanocrystal for thermoelectric energy conversion has been investigated by Fang et al. [23]. In this paper, electrochemical properties of pure Te nanoparticles for supercapacitor and biosensor applications have been accounted.

2 Methods

2.1 Synthesis procedure

Tellurium dioxide powder (TeO_2, 99%), hydrazine monohydrate ($N_2H_4.H_2O$, 80%) and sodium dodecyl sulfate (SDS, $C_{12}H_{25}O_4SNa$, 99%) were purchased from Sigma Aldrich. Deionized water from a Milli-Q ultrapure (18.2 MΩ-cm^{-1}) was used. The details of the synthesis procedure are described elsewhere [24]. TeO_2 powder was dissolved in 10 ml of $N_2H_4.H_2O$ under magnetic stirring at 303 K. The colour of the solution continuously changed from amber to purple and then to blue. The blue indicates the formation of t-Te Nps. The solution was diluted with SDS (10 mM) to stabilize the prepared t-Te Nps. The final solution was centrifuged several times with double distilled water to remove the impurity of the matrices such as SDS and hydrazine monohydrate and the obtained t-Te powder was dried at 303K.

2.2 Material characterization

XRD pattern was recorded (PANalytical X-pert pro) with CuKα (1.5406Å) in the 2θ range from 20 to 80°and micro raman spectrum (Witec Confocal CDM 200) was recorded with 488 nm laser excitation. FESEM image (Hitachi High Tech SU 6600) and TEM image (FEI-Tecnai microscope equipped with a LaB6 filament at an operating voltage of 200 kV) were taken. XPS was recorded on (SPECS PHOIBES$_{100}$ MCD ANALYSER ELECTRODE ALUMINIUM K ALPHA (1486.6 eV at 40 eV pass energy). Optical properties like absorption and emission were studied using UV-Visible (Shimadzu 1800) and fluorescence (Floromax) spectrophotometers. Cyclic voltammetry (CV) and amperometric analyses were performed using (BioLogic SP-150) electrochemical workstation.

2.3 Electrochemical measurement

2.3.1 Fabrication of electrode for energy storage device

The active material Te, activated carbon and polytetrafluro-ethylene were mixed (80:15:5) with the addition of ethanol. The slurry was coated on to a graphite sheet of area 1cm^2. The electrochemical experiment (CHI 660D electrochemical workstation) was carried out using

a single compartment three–electrode system with Te as a working electrode, platinum as a counter electrode and Ag/AgCl as the reference electrode with 2 M KOH as electrolyte. The charge and discharge characterizations were performed at current densities from 2 to 30 mA/cm^2 within a potential window of -1.0 to 0.2 V.

2.3.2 Fabrication of electrode for biosensor

All the measurements were recorded using three electrodes set up at 303 K. In the three electrode system, glassy carbon electrode (GCE) as a working electrode, Ag/AgCl as a reference electrode and Pt wire as a counter electrode were used. Phosphate buffer solution (PBS) was prepared as an electrolyte. For preparing Te Nps modified GCE (TNPCGEs) electrode, 1mg of Te powder was first dispersed in 50 µL of Nafion solution and then in 0.5 mL of ethanol and sonicated for 30 min. 5 µL of the dispersed solution was dropped on GCE electrode, dried in atmospheric air and the modified electrode was used for H_2O_2 sensing. The following equations describe the mechanism of sensing. Oxidation involves the reaction of Te with H_2O with the release of electrons. Correspondingly in the reduction process, TeO_2 reduces H_2O_2 to water. [16]

$$Te + 2H_2O \rightarrow TeO_2 + 4H^+ + 4e^- \quad \text{(Oxidation)} \qquad (1)$$

$$TeO_2 + 2H_2O_2 \rightarrow Te + 2H_2O + 2O_2 \quad \text{(Reduction)} \qquad (2)$$

Before the electrochemical measurements, TNPCGEs were electrochemically treated by 10 cycles of CV in PBS (10 mM, pH 7.0) over the potential range of -1.5 to 1.5V at scan rates such as 20, 40, 60, 80 and 100 mVs^{-1} to remove the unwanted materials from the TNPCGEs. The selectivity and sensitivity towards H_2O_2 were verified by conducting CV over the same potential range at a scan rate of 40 mVs^{-1}. The interference test and the detection of H_2O_2 were performed under the same range in the presence of oxalic acid (OA) and ascorbic acid (AA) obtained by CA at an applied potential of -0.4V.

The surface of GCE was polished, washed and electrochemically pre-treated by CV between -1.5 to 1.5V in PBS. The area of the effective surface is determined by the Randles-Sevcik equation.

$$I_p = (2.69\times10^5)n^{3/2}\times A\times D^{1/2}\times C\times \upsilon^{1/2} \quad (2)$$

Where I_p is the peak current of the redox couple (A), n is the number of electrons, A is the area of the electrode (cm^2), the diffusion coefficient D of the molecule in solution (cm^2s^{-1}), C is the concentration of the bulk solution in mol (cm^{-3}) and υ is the scan rate in ($V\ s^{-1}$), using the above equation in which I_p is proportional to $\upsilon^{½}$, an approximate value of A is obtained [25].

3. Results and Discussion

3.1 Structural and Morphological

XRD pattern corresponds to the hexagonal phase of Te with space group $P3_121$ (JCPDS, 36-1452) (Fig. 1a) and the lattice constants are a = 0.4459 and c = 0.5902 nm [26]. A strong peak at 2θ = 27° is due to the reflection from (101) plane and is the characteristic peak of t-Te. No impurity diffraction peaks are detected indicating the high purity of the product with a preferential growth along [001]. The crystallite size (34 nm) is estimated using Debye Scherrer's equation

$$D = \frac{0.9\lambda}{\beta\cos\theta} \quad (3)$$

The two strong peaks at 123 and 148 cm^{-1} in the micro Raman spectrum given in fig. 1b are attributed to the A_1 and E phonon modes of vibration. Similar peaks (122.5 and 140.2 cm^{-1}) were reported by Liu et al. [20] for Te nanowires. But, in the case of hydrothermally synthesized Te nanotubes in a tungstosilicate acid solution, the same band assignment is reported for 119.7 and 135.4 cm^{-1} [27]. FESEM micrograph shows the nanoparticles of spherical shape (Fig. 2a). Following the same synthesis route, Suchand et al. [2] have discussed Te nanowires with a length and width of 600 and 20 nm respectively. The average particle size of Te NPs from TEM image (fig. 2b) is found to be 307 nm. But for the same synthesis procedure and conditions, nanowires of length ≈ 456 nm, increasing with the stirring time is accounted [24]. Fig. 2c depicts the lattice resolved TEM image of Te NPs. The interplanar spacing corresponding to (101) plane of Te is found to be 0.323 nm. The crystallinity and orientation of the NPs are confirmed from SAED pattern which are consistent with the hexagonal structure of Te (Fig. 2d). As the EDX

spectrum (fig. 2e) shows only the presence of Te, the formation of elemental Te is verified. Fig. 3a presents the survey of XPS for Te and the binding energy of Te 4d, 4p, 4s, $3d_{5/2}$, $3d_{3/2}$, $3p_{3/2}$ and $3p_{1/2}$ states are 43, 112, 172, 575.9, 586.3, 822 and 873 eV respectively. The presence of other elements like C1s, O1s and MNN Auger lines are found at 282, 531and 1008 eV respectively. The binding energy $3d_{5/2}$ and $3d_{3/2}$ states of pure Te are reported as 572.7 and 583.1 eV [28, 29]. In the present case as Te is easily oxidized in air, there is a possibility for the formation of Te (IV) and a corresponding shift in the peak positions at 575.9 and 586.3 eV is observed. The enlarged view of 3d region is shown in fig. 3b.

3.2 Optical properties

Absorption spectrum of Te contains two characteristics peaks, one in the range of 250-350 nm and another in 600-850 nm. The former one is due to the p-bonding valence band to the p-antibonding conduction band transition and latter is due to the p-lone pair valence band to the p-antibonding conduction band [30]. In the present case (Fig. 4), the peak positions are 340 nm (3.6 eV) and 670 nm (1.85 eV). For Ag_2Te nanowires [2], a single absorption peak at 480 nm (2.58 eV) is reported which is favorable in the construction of broadband optical limiters. For an excitation wavelength of 290 nm, the fluorescence emission spectrum is given in the inset of fig. 4. The deconvolution of the broad emission peak produces three Gaussian peaks centered at 396, 437 and 467 nm in the blue-violet region with an excitation wavelength of 363 nm. Similar emissions are noticed for Te nanowires for an excitation of 265 nm. t-Te nanotubes show an intensive peak at 458 nm [26] whereas Gautam et al. [31] have reported a broad emission band at 700 nm for Te nanorods.

3.3 Electrochemical studies

3.3.1 Cyclic voltammetry

Fig. 5a shows the CV of Te electrode for different scan rates 5, 10, 25, 50 and 100 mVs^{-1} in the potential range of -1.0 to 0.2 V using 2 M KOH as the electrolyte. The oxidation process of the Te electrode was detected through the ion intercalation and de-intercalation of K^+ in the Te active material.

CV curves exhibit well defined oxidation peak and confirm the Faradic nature of the material alternative to pseudocapacitive behavior. The oxidation peak current increases linearly with the scan rate indicating the supercapacitance behavior of Te Nps. The inset shows the linear relationship between anodic peak current and square root of the scan rate, due to the redox reaction through adsorption of hydroxyl ions in alkaline electrolyte at the electrode interface [32]. It is seen that there is a little change in the oxidation potential of the electrode material during K^+ insertion and extraction for different scan rates. The specific capacitance (C_s) is calculated

$$C_s = \frac{Q}{m\Delta V} F / g \qquad (4)$$

where Q is the average charge during anodic and cathodic scan, m is the mass of active material and ΔV is the applied voltage window [33]. The specific capacitance for scan rates 5, 10, 25, 50 and 100 mVs^{-1} are 125.8, 93.2, 63.9, 48.6 and 35.3 F/g respectively. At lower scan rates, the higher surface area of the electrode improves the utilization rate during the electrochemical redox process and therefore a higher capacitance is found (Fig. 5b). The specific capacitance decreases as the scan rate increases, indicating a good rate capability of Te electrode. For a scan rate of 20 mVs^{-1}, a high specific capacitance of 930 F/g is attributed to the hybrid core shell structure [8]. But Te nanowires reduced from bulk Bi_2Te_3 through electrolysis show a supercapacitance of 24 F/g for a scan rate of 25 mVs^{-1} lower than the present study (64 F/g) [34].

3.3.2 Chronopotentiometry

The galvanostatic charge-discharge measurement was carried out between -1.0 and 0.2 V at current densities from 2 to 30 mA/cm^2. The observed charging curve is almost similar to discharging curve but slightly differ from the charging time (Fig. 5c). The shape of the curves shows an ideal pseudocapacitive behavior with sharp response and small internal resistance (IR) drop. The specific capacitance (C_s) is evaluated

$$C_s = \frac{I\Delta t}{m\Delta V} F / g \qquad (5)$$

where I is the discharging current, Δt is the discharge time, m is the mass of active material and ΔV is the applied potential window [35]. Fig. 5d shows a visible decrease of the capacitance from 586 to 100 F/g with an increase in the current density from 2 to 30 mA/cm^2. A high specific capacitance for a low current density is due to the fast charge transfer at the interface of the electrode and the electrolyte. At higher current density, the hydrate ions block the dynamic accommodation of the electrode surface, resulting in lower capacitance confinement. Due to the limited movement of K^+ ions in the electrode, the charging process is difficult as the charging current density increases. The specific capacitance (C_s) values obtained from both the techniques (charge/discharge and cyclic voltammetry) are comparable. Energy (E) and power (P) densities are calculated and the Ragone plot is drawn (Fig. 5e).

$$E = \frac{1}{2} C_s \times (\Delta V)^2 \tag{6}$$

$$P = \frac{E}{t} \tag{7}$$

where C_s is the specific capacitance, ΔV is the potential window and t is the discharging time. As E decreases from 116 to 19 Whkg^{-1}, P increases from 1186 to 17100 Wkg^{-1} with an increase of current density from 2 to 30 mA/cm^2. This is much similar to the conventional supercapacitors in Ragone plots. The electrochemical utilization of Te electrode (Z) is evaluated

$$Z = C_s . \Delta V . \frac{M}{F} \tag{8}$$

where C_s is the specific capacitance (F/g), ΔV is the potential window (1.2 V), M is the atomic weight of Te (127.60 g) and F is the Faradic constant (96485) [36]. Z value is 1 for all the electroactive materials involved in the Faradic reaction. The equation gives 0.9299 to 0.1586 of Z values for current density of 2, 5, 10, 20, 30 mA/cm^2 for Te Nps. This means that at a current density of 2 mA/cm^2, 92.99% of electroactive sites are involved in the redox process. The specific capacitance value is enhanced to 586 F/g at a current density of 2 mA/cm^2 while the same for a current density of 30 mA/cm^2 is 100 F/g. At low current density, as the ions access the outer surface as well as the inner pores, the specific capacitance became high. But at high

values, the ions did not get enough time to intercalate and deintercalate, consequently the specific capacitance decreases. The cyclic stability (η) is given by

$$\eta = \frac{t_c}{t_d} \times 100 \qquad (9)$$

where t_c and t_d are the charge and discharge intervals and it is found to be 100% (Fig. 5f) for 1000 cycles with current density of 30 mA/cm^2 [37]. Even after the 1000th cycle, the specific capacitance is remained as 100 F/g. Electrochemical capacitor behavior of CuS nanoplates is reported with a specific capacitance, energy density, power density and cyclic stability of 72 F/g, 6.226 Whkg$^{-1,}$ 1750 Wkg^{-}1 and 36.29% respectively [38]. A cyclic stability of 98.6% is obtained for a current density of 5 mA/cm^2 whereas the specific capacitance varies from 555 to 464 F/g for a current density from 5 to 100 mA/cm^2 in the case of cobalt sulfide hierarchitectures [39]. The obtained values of supercapacitance and cyclic stability in the present study are found to be comparable with the reported work as listed in table 1.

3.3.3 Electrochemical impedance spectroscopy

Fig. 6a shows the Nyquist plot in a three electrode mode at the frequency range of 0.01 – 100 KHz with amplitude (5 mV) and bias potential (0.7 V). The frequency dependent specific capacitance [40] is given by

$$C_s = \frac{1}{2\pi f z''} \qquad (10)$$

The calculated value from the impedance data for the Te electrode is presented in fig. 6b. The impedance spectrum of the supercapacitor shows solution resistance R_s is 6.043 Ω and in the mid-high frequency region and the charge transfer resistance R_{ct} is 0.001 Ω. An incident line in the low frequency range is considered as the Warburg constant (W) which is found to be 0.0891, associated with the diffusion of K^+ ions into Te electrode and the calculated C_S value is 610 F/g (at 0.01 Hz for 0.7 V). For Co_3O_4 Nps, the R_s, R_{ct} and C_s values are 1.09 Ω, 0.5 Ω and 532 F/g respectively [40]. Also R_s, R_{ct} and W of 0.09 Ω, 0.3 Ω and 0.4 respectively are reported for La_2Te_3 film from electrochemical impedance spectroscopy [41].

3.3.4 Biosensor

The electrochemical characteristics of Te NPs were analyzed through CV using Nafion as a binder in deoxygenates PBS. Fig. 7a gives the voltammograms recorded on GCE bare (curve a), Te/GCE (curve b) and Te/GCE/Nafion (curve c) at a sweep rate of 40 mV s^{-1} between -1.5 to 1.5V range. GCE bare electrode shows E_{pa} at 0.29 V and 0.44 V in the presence of Te and it shows 0.44 V (oxidation), -0.87 and -1.04 V (reduction) in presence of Te/GCE/Nafion.

"The oxidation and reduction processes observed in the CV are explained as follows:

$$Te + 2H_2O \leftrightarrow TeO_2 + 4H^+ + 4e^- \quad (E_{pa} = 0.44 \text{ V in oxidation})$$

$$TeO_2 + 4H^+ + 4e^- \rightarrow Te + 2H_2O \quad (E_{pc} = -0.8 \text{ V in reduction})"$$

The observed oxidation and reduction peaks (Te) in the CV matches well with the previously reported oxidation and reduction potential for Te thin films [42, 43]. Therefore we observed that redox potential values are comparable with previous report.

Fig. 7b illustrates the CV for Te/GCE/Nafion in deoxygenated PBS at scan rate from 20 to 100 mV s^{-1} in the same potential range. Both the redox peak current and peak-to-peak separation increase with the scan rate [44]. With the increase of scan rate, a shift in both anodic and cathodic peak current is observed (fig. 7c). In order to confirm the electrode process, a graph is drawn between peak current (I_p) versus scan rate (υ), and the obtained graph is a straight line in the range of -1.5 to 1.5 V with correlation coefficient (r^2) 0.9723 and 0.7552. The I_p versus square root of scan rate ($\upsilon^{1/2}$) were plotted as shown in fig. 7d with correlation coefficient (r^2) 0.8859 and 0.9025. This suggests an adsorption-controlled electrode process [45]. The variation of E_{pa} and E_{pc} as a function of log (v) for Te peak pairs. A linear dependence is visible for both the peaks as expected for a totally irreversible surface process.

In relation to this model, a graph of E_{pa} = f(log v) yields a straight line with a slope equal to 2.3RT/αnF and the intercept (2.3RT/αnF)log(αnF/RTks)+E_{surf} for the cathodic peak (eqn. 11). For the anodic peak, the slope is 2.3RT/(1-α)nF with the intercept [2.3RT/(1-α)nF]log[(1-α)nF/RTks]+E_{surf} (eqn. 12) [15].

$$E_{pc} - E_{surf} = \left(\frac{-2.3RT}{\alpha nF}\right)\log v - \left(\frac{2.3RT}{\alpha nF}\right)\log\left(\frac{\alpha nF}{RTks}\right) \quad (11)$$

$$E_{pa} - E_{surf} = \left(\frac{2.3RT}{(1-\alpha)nF}\right)\log v - \left(\frac{2.3RT}{(1-\alpha)nF}\right)\log\left(\frac{(1-\alpha)nF}{RTks}\right) \quad (12)$$

The electrode transfer rate constant (k_s) for Te/GCE/Nafion was calculated using Laviron's equation (13) [46].

$$\log k_s = \alpha\log(1-\alpha) + (1-\alpha)\log\alpha - \log\left(\frac{RT}{nFv}\right) - \frac{nF\Delta E_{pa}(1-\alpha)}{2.3RT} \quad (13)$$

Where α value is assumed as 0.5, R is the gas constant, T is the room temperature, ΔE_{pa} is the peak separation of redox potential and the number of electrons transferred n is 1. The k_s value at Te/GCE/Nafion is calculated to be 1.0237 s^{-1} and it is higher than the values of the interface behavior of hemoglobin at carbon nanotubes (0.062 s^{-1}) [47] and silica gold nanorods (0.83 s^{-1}) [48]. These results indicate the Te gives fast electron transfer rate from the electrode surface of for H_2O_2. Fig 7e reveals the CV of the Te/GCE/Nafion in the presence and absence of of 1 mM H_2O_2 at 40 mV s^{-1} in PBS. It is observed that the reduction peak current value was increased in the presence of H_2O_2. Figure 7f shows the CV sensing of H_2O_2 by successive addition of 0.67 µM. it is observed that on increasing the concentration of HP reduction peak current values are decreased linearly at a potential value of ~-0.8 V.

3.3.5 Amperometry sensing

CA response to H_2O_2 is depicted in the fig. 8a. While maintaining PBS in a stirring condition, different concentrations of H_2O_2 are added at regular intervals. The CA analysis was studied on the chemically modified electrode by applying constant potential of -0.4 V. The Te/GCE/Nafion exhibit a wide linear range of 0.67 – 8.04 µM with the correlation coefficient 0.9956 with the addition of H_2O_2 into the electrolyte solution and the catalytic current increases and reaches its steady state within 5s (fig. 8b). The Te sensor displays a sensitivity of 0.83 mA mM^{-1} cm^{-2} with a limit of detection 0.3 µM and the observed value are enhanced as compared with previous report for nonenzymatic hydrogen peroxide. Reported values are tableted in 2. The

selectivity has been determined by monitoring the amperometric response after consecutive injection of 0.67 µM H_2O_2, AA and OA at an applied potential of -0.4 V. However, a rapid increase in the current is observed by the addition of H_2O_2. It is evident that the sensor does not exhibit a significant response to both AA and OA than H_2O_2 (fig 8c). It indicates the high selectivity of the proposed sensor.

4. Conclusion

Te Nps synthesized by wet chemical method are found to be in hexagonal phase with spherical morphology (307 nm). Due to unique fluorescence properties, the prepared Te NPs facilitates the fabrication of optoelectronics devices. When applied as an electrode for super capacitor, Te Nps exhibit better electrochemical performances with specific capacitance of 100 F/g at a current density of 30 mA/cm^{-2} and 100% cyclic stability after 1000th cycle. In addition, the amperometric response indicates that the as-prepared Te/GCE/Nafion nanoparticle is able to enhance the electocatalytic properties of the electrode for H_2O_2 in CV experiment. Te NPs exhibit high sensitivity, short response time with a wide linear range of H_2O_2 in PBS for chronoamperometric experiments. These results are promising for the next generation energy storage devices and biosensors.

References

[1] J. Choi, J. Y. Lee, H. Lee, C. R. Park, H. Kim, Enhanced thermoelectric properties of the flexible tellurium nanowires film hybridized with single-walled carbon nanotubes, *Synth. Met.,* **198** (2014) 340-344.

[2] C. S. Sandeep, A. K. Samal, T. Pradeep, R. Philip, Optical limiting properties of Ag_2Te nanowires, *Chem. Phys. Lett.* **485** (2010) 326-330.

[3] Z. Wang, L. Wang, J. Huang, H. Wang, L. Pan, X. Wei, Formation of single-crystal tellurium nanowires and nanotubes via hydrothermal recrystallization and their gas sensing properties at room temperature, *J. Mater. Chem.,* **20** (2010) 2457-2463.

[4] Y. Fan, L. Jiang, J. Yang, Y. Jiang, F. Liu, The electrochemical behavior of tellurium on stainless steel substrate in alkaline solution and the illumination effects, *J. Electroanal. Chem.,* **771** (2016) 17-22.

[5] E. Rudnik, J. Sobesto, Cyclic voltammetric studies of tellurium in diluted HNO_3 solutions,

Arch. Metall. Mater., **56** (2011) 271-277.

[6] R. R. Bi, X. L. Wu, F. F. Cao, L. Y. Jiang, Y. G. Guo, L. J. Wan, Highly dispersed RuO_2 on carbon nanotubes: Facile synthesis and enhanced supercapacitor performance, *J. Phys. Chem. C* **114** (2010) 2448-2451.

[7] Y. Liu, J. Wang, Y. Xu, Y. Zhu, D. Bigio, C. Wang, Lithium-tellurium batteries based on tellurium/porous carbon composite, *J. Mater. Chem. A* **2** (2014) 12201-12007.

[8] J. Cao, M. Safdar, Z. Wang, J. He, High-performance flexible supercapacitor electrodes based on Te nanowire arrays, *J. Mater. Chem. A* **1** (2013) 10024-120029.

[9] H. W. Tsai, A. Yaghoubi, T. C. Chan, C. C. Wang, W. T. Liu, C. N. Liao, S. Y. Lu, L. J. Chen, Y. L. Chueh, Electrochemical synthesis of ultrafast and gram-scale surfactant-free tellurium nanowires by gas-solid transformation and its applications on supercapacitor electrodes and p-doping of graphene transistor, *RSC Nanoscale* **7** (2015) 7535-7539.

[10] K. Fang, Y. Yang, L. Fu, H. Zheng, J. Yuan, L. Niu, Highly selective H_2O_2 sensor based on 1-D nanoporous Pt@C hybrid with core-shell structure, *Sens. Actuators B* **191** (2014) 401-407.

[11] T. Zheng, X. Li, X. Bian, C. Zhang, Y. Xue, X. Jia, C. Wang, Fabrication of ternary CNT/PPy/K_xMnO_2 composite nanowires for electrocatalytic Applications, *Talanta* **90** (2012) 51-56.

[12] W. Jia, M. Guo, Z. Zheng, T. Yu, E. G. Rodriguez, Y. Wang, Y. Lei, Electrocatalytic oxidation and reduction of H_2O_2 on vertically aligned Co_3O_4 nanowalls electrode: towards H_2O_2 *J. Electro. Chem.* **625** (2009) 27-32.

[13] X. Li, X. Liu, W.Wang, L. Li, X. Lu, High load Pt nanoparticles on functionalized of carbon nanotubes for fabricating nonenzyme hydrogen peroxide sensor, *Biosens. Bioelectron.* **59** (2014) 221-226.

[14] M. R. Guascito, E. Filippo, C. Malitesta, D. Manno, A. Serra, A. Turco, A new amperometric nanostructured sensor for the analytical determination of hydrogen peroxide, *Biosens. Bioelectron.* **24** (2008) 1057-1063.

[15] M. R. Guascito, D. Chirizzi, C. Malitesta, T. Siciliano, A. Tepore, Te oxide nanowires as advanced materials for amperometric nonenzymatic hydrogen peroxide sensing, *Talanta* **115** (2013) 863-869.

[16] M. R. Guascito, D. Chirizzi, C. Malitesta, E. Mazzotta, M. Siciliano, T. Siciliano, A. Tepore, A. Turco, Low-potential sensitive H_2O_2 detection base on the composite microtubular Te absorbed on platinum electrode, *Biosens. Bioelectron.* **26** (2011) 3562-3569.

[17] M. R. Guascito, D. Chirizzi, C. Malitesta, M. Siciliano, T. Siciliano, A. Tepore, Amperometric non-enzymatic bimetallic glucose sensor based on platinum tellurium microtubes modified electrode, *Electrochem. Commun* **22** (2012) 45-48.

[18] H. Y. Tsai, Z. H. Lin, H. T. Chang, Tellurium-nanowire-coated glassy carbon electrodes for selective and sensitive of dopamine, *Biosens. Bioelectron.* **35** (2012) 479-483.

[19] X. Wu, Y. Wang, S. Zhou, X. Y. Yuan, T. Gao, K. Wang, S. Lou, Y. Liu, X. Shi, Morphology control, crystal growth and growth mechanism of hierarchical tellurium (Te) microstructures, *Cryst. Growth & Des.* **13** (2013) 136-142.

[20] J. W. Liu, F. Chen, M.Zhang, H. Qi, C. L. Zhang, S. H. Yu, Rapid microwave-assisted synthesis of uniform ultralong Te nanowires, optical property and chemical stability, *Langmuir* **26** (2010) 11372-11377.

[21] Q. Lu, F. Gao, S. Komarneni, Biomolecule-assisted reduction in the synthesis of single-crystalline tellurium nanowires, *Adv Mater.* **16** (2004) 1629-1632.

[22] L. Hou, Q. Zhang, L. Ling, C. X. Li, L. Chen, S. Chen, Interfacial fabrication of single-crystalline ZnTe nanorods with high blue fluorescence, *J. Am. Chem. Soc.* **135** (2013) 10618-10621.

[23] H. Fang, Z. Luo, H. Yang, Y. Wu, The effect of the size and the doping concentration on the power factor of n-type lead telluride nanocrystal for thermoelectric energy conversion, *Nano Lett.* **14** (2014) 1153-1157.

[24] Z. H. Lin, Z. Yang, H. T. Chang, Preperation of fluorescent tellurium nanowires at room temperature, *Cryst. Growth & Des.* **8** (2008) 351-357.

[25] M. J. Song, S. W. Hwang, D. Whang, Amperometric hydrogen peroxide biosensor based on a modified gold electrode with silver nanowires, *J. Appl. Electrochem*. **40** (2010) 2099-2105.

[26] J. M. Song, Y. Z. Lin, Y. C. Tian, G. Liu, S. H. Yu, Superlong high-quality tellurium nanotubes: synthesis, characterization and optical property, *Cryst. Growth & Des.* **8** (2008)

1902-1908.

[27] L. Zhang, C. Wang, D. Wen, preparation by hydrothermal techniques in a tungstosilicate acid solution system and optical properties of tellurium nanotubes, *Eur. J. Inorg. Chem.* **22** (2009) 3291-3297.

[28] J. W. Liu, J. H. Zhu, C. L. Zhang, H. W. Liang, S. H. Yu, Mesostructured assemblies of ultrathin superlong tellurium nanowires and their photoconductivity, *J. Am. Chem. Soc*. **132** (2010) 8945-8952.

[29] H. W. Zhang, M. T. Swihart, synthesis of tellurium dioxide nanoparticles by spray pyrolysis, *Chem. Mater*. **19** (2007) 1290-1301.

[30] T.S. Sreeprasad, A.K. Samal, T. Pradeep, Tellurium nanowires-induced room temperature conversion of graphite oxide to leaf-like graphenic structures, *J. Phys. Chem.* **113** (2009) 1727-1737.

[31] U.K. Gautam, C.N.R. Rao, Controlled synthesis of crystalline tellurium nanorods, nanowires, nanobelts and related structures by a self-seeding solution process, *J. Mater. Chem.* **14** (2004) 2530-2535.

[32] C. Gong, M. Huang. P. Zhou, Z. Sun, L. Fan, J. Lin, J. Wu, Mesoporous $Co_{0.85}Se$ nanosheet supported on Ni foam as a positive electrode material for asymmetric supercapacitor, *Appl. Surf. Sci.* **362** (2016) 469-476.

[33] S. M. Chen, R. Ramachandran, V. Mani, R. Saraswathi, Recent advancements in electrode materials for the high-performance electrochemical supercapacitor: a review *J. Electrochem. Sci.* **9** (2014) 4072-4085.

[34] H. W. Tsai, A. Yaghoubi, T. C. Chan, C. C. Wang, W. T. Liu, C. N. Liao, S. Y. Lu, L. J. Chen, Y. L. Chueh, Electrochemical synthesis of ultrafast and gram-scale surfactant-free tellurium nanowires by gas-solid transformation and its applications on supercapacitor electrodes and p-doping of graphene transistor, *RSC Nanoscale* **7** (2015) 7535-7539.

[35] S. Vijayakumar, S. Nagamuthu, G. Muralidharan, Supercapacitor studies on NiO nanoflakes synthesized through a microwave route, *ACS Appl. Mater. Interfaces* **5** (2013) 2188-2196.

[36] K. W. Nam, K. B. Kim, A study of the preparation of NiO_x electrode via electrochemical route for supercapacitor applications and their charge storage mechanism, *J. Electrochem.*

Soc. **149** (2002) A346-354.

[37] W. Du, Z. Zhu, Y. Wang, J. Liu, W. Yang, X. Qian, H. Pang, One-step synthesis of $CoNi_2S_4$ nanoparticles for supercapacitor electrodes, *RSC Adv.* **4** (2014) 6998-7002.

[38] C. Justin Raj, B. C. Kim, W. J. Cho, W. G. Lee, Y. Seo, K. H. Yu, Electrochemical capacitor behavior of copper sulfide (CuS) nanoplates, *J. Alloys Compd*. **586** (2014) 191-196.

[39] Q. Wang, L. Jiao, J. Yang, Q. Huan, W. Peng, Y. Si, Y. Wang, H. Yuan, Facile synthesis and superior supercapacitor performances of three-dimensional cobalt sulfide hierarchitectures *Cryst. Eng. Comm.* **13** (2011) 6960-6963.

[40] S. Vijayakumar, A. Kiruthika Ponnalagi, S. Nagamuthu, G. Muralidharan, Microwave assisted synthesis of Co_3O_4 nanoparticles for high performance supercapacitors, *Electrochim. Acta* **106** (2013) 500-505.

[41] S. J. Patil, B. H. Patil, R. N. Bulakhe, C. D. Lokhande, Electrochemical performance of a portable asymmetric supercapacitor device based on cinnamon-like La_2Te_3 prepared by a chemical synthesis route, *RSC Adv.* **4** (2014) 56332-56341.

[42] W. Zhu, J. Y. Wang, X. H. Gao, J. Hou, S. Q. Bao, X. A. Fan. The underpotential deposition of bismuth and tellurium on cold rolled silver substrate by ECALE, *Electrochim. Acta* **20** (2005) 5465-5472.

[43] K. K Mishra, D. Ham, K. Rajeshwar, Anodic oxidation of telluride ions in aqueous base: a rotating ring-disk electrode study, J. Electrochem. Soc. **137** (2009) 3438-3441.

[44] S. Palanisamy, S. Cheemalapati, S. M. Chen, Highly sensitive and selective hydrogen peroxide biosensor based on hemoglobin immobilized at multiwalled carbon nanotubes-zinc oxide composite electrode, *Anal. Electrochem.* **429** (2012) 108-115.

[45] P.S. Ganesh, B.E. Kumara Swamy, Simultaneous electroanalysis of norepinephrine, ascorbic acid and uric acid poly (glutamic acid) modified carbon paste electrode, *J. Electroanal. Chem*. **752** (2015) 17-24.

[46] Z. W. Xuan, X. Y. Sun, G. S. Jiao, Z. Q. Zhai, W. Sun, L. Lu, Ionic liquid-hemoglobin-carbon paste composite bioelectrode and its electrocatalytic activity, *J. of Chinese Chem. Soc*. **57** (2010) 1262-1267.

[47] Y. D. Zhao, Y. H. Bi, W. D. Zhang, Q. M. Luo, The interface behavior of hemoglobin at

carbon nanotubes and the detection for H_2O_2, *Talanta* **65** (2005) 489-494.

[48] J. J. Zhang, Y. G. Liu, L. P. Jiang, J. J. Zhu, Synthesis characterizations of silica-coated gold nanorods and its applications in electroanalysis of hemoglobin, *Electrochem. Commun*. **10** (2008) 355-358.

[49] S. J. Patil, B. H. Patil, R. N. Bulakhe, C. D. Lokhande, Electrochemical performance of a portable asymmetric supercapacitor device based on cinnamon-like La_2Te_3 prepared by a chemical synthesis route, *RSC Adv.* **4** (2014) 56332-56341.

[50] D. Chakravarty, P. Kumar, V. S. Ugale, D. J. Late, Microwave- assisted synthesis of few-layered $TaTe_2$ and its application as supercapacitor, *Eur. J. Inorg. Chem.* **9** (2015) 1-7.

[51] J. Sophia, G. Muralidharan, Polyvinylpyrrolidone stabilized palladium nanospheres as simple and novel electrochemical sensor for amperometric hydrogen peroxide detection, J. Electroanal. Chem. **739** (2015) 115-121.

[52] S. Yao, J. Xua, Y. Wang, X. Chen, Y. Xu, S. Hu, A highly sensitive hydrogen peroxide amperometric sensor based on MnO_2 nanoparticles and dihexadecyl hydrogen phosphate composite film, Anal. Chim. Acta 557 (2006) 78-84.

Tables

Table: 1 supercapacitance and cyclic stability of various telluride electrodes.

S.No	Materials	Electrolyte	Specific capacitance (F/g)	Cyclic Stability (%)	Ref.
1	Te/Au/MnO_2	0.1 M Na_2SO_4	930	97	8
2	Te NWs	0.5 M Na_2SO_4	23	46	9
3	La_2Te_3	1 M KOH	63	71	49
4	$TaTe_2$	0.5 M KOH	4	95	50
5	Te Nps	2 M KOH	100	100	Present work

Table: 2 Comparison of various chalcogenides based non-enzymatic amperometric H_2O_2 sensor

S.No	Sensor	Sensitivity (cm^{-2})	LOD	Applied potential (V)	Ref.
1	PtPNW@C	0.35 µA $µM^{-1}$	0.1 µM	0.2	10
2	Co_3O_4	100.3µA mM^{-1}	2.8 µM	0.8	12
3	Pd Sps embedded in PVP	331 µA mM^{-1}	4.3 µM	-0.02	51
4	Nano MnO_2/DHP	84.4 µA mM^{-1}	0.12-2.16	-0.25	52
5	GCE/Te/Nafion Nps	0.83 mA $µM^{-1}$	0.3 µM	-0.4	Present work

Figures

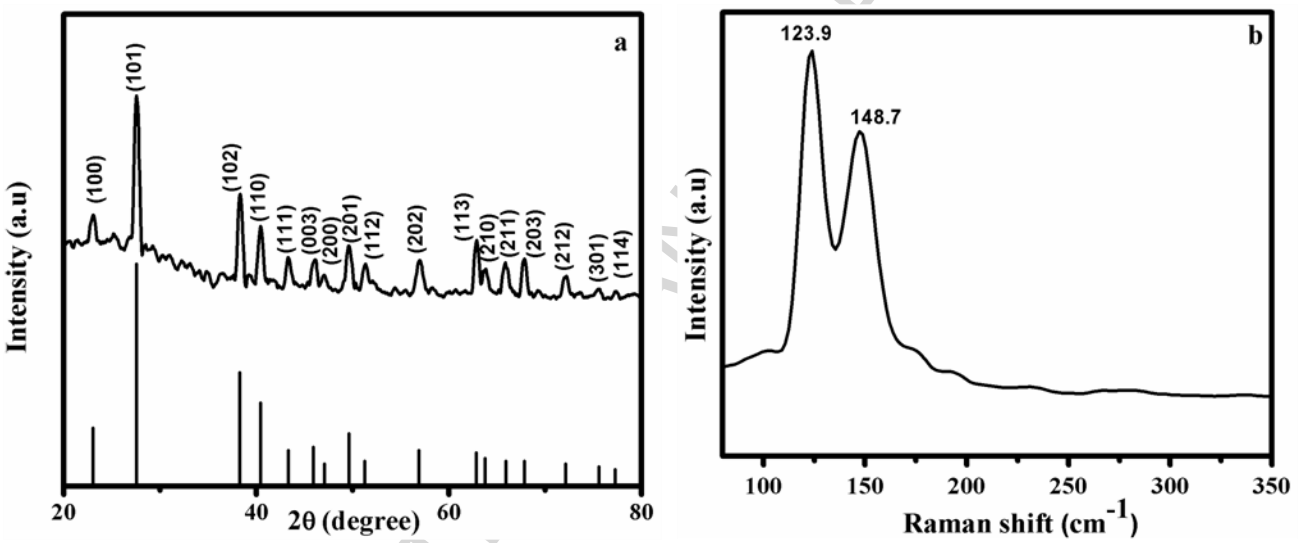

Fig. 1 (a) Powder XRD pattern of Te Nps, (b) Micro-Raman spectrum of Te Nps.

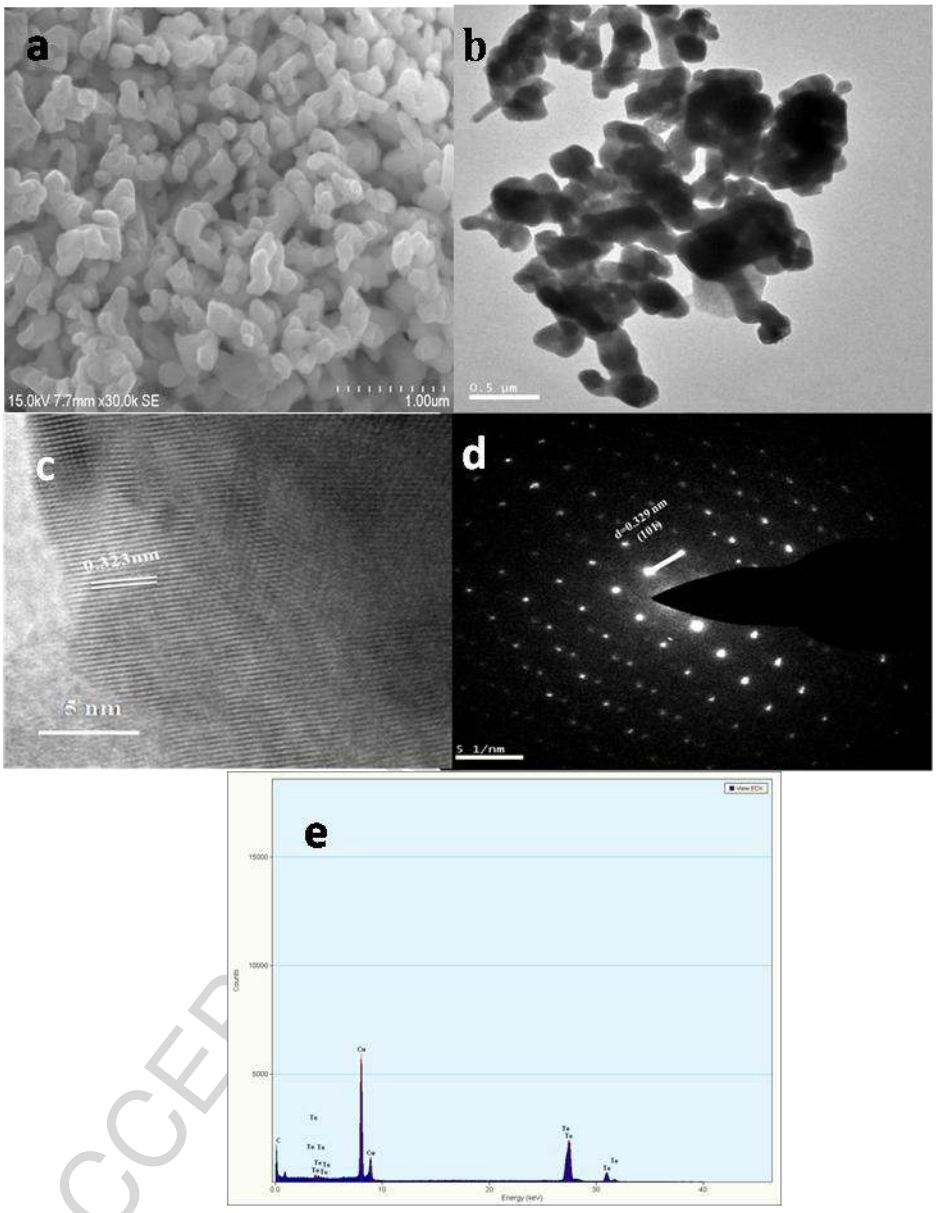

Fig 2 (a) FESEM (b) TEM (c) lattice-resolved TEM (d) SAED pattern of TEM image (e) EDX spectrum for Te Nps.

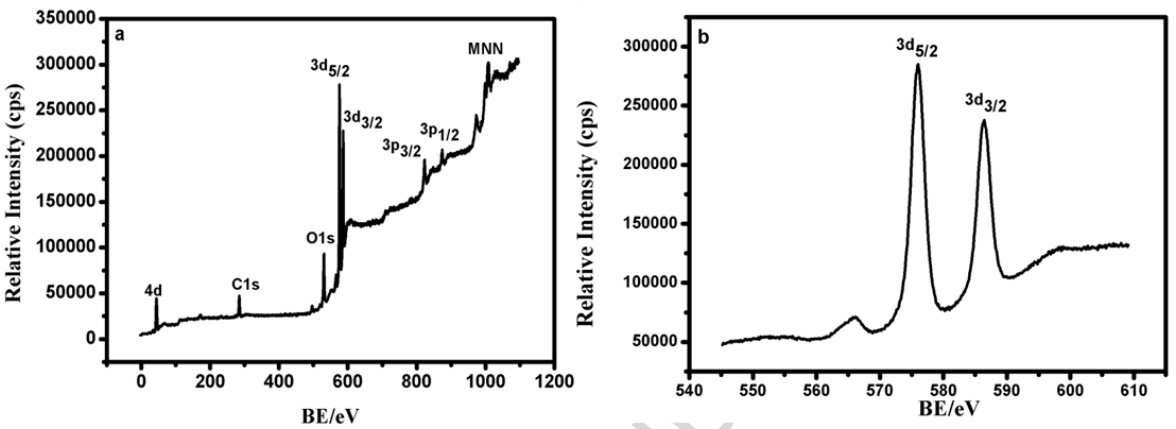

Fig. 3 (a)XPS spectrum for Te Nps (b) Survey of the Te 3d region

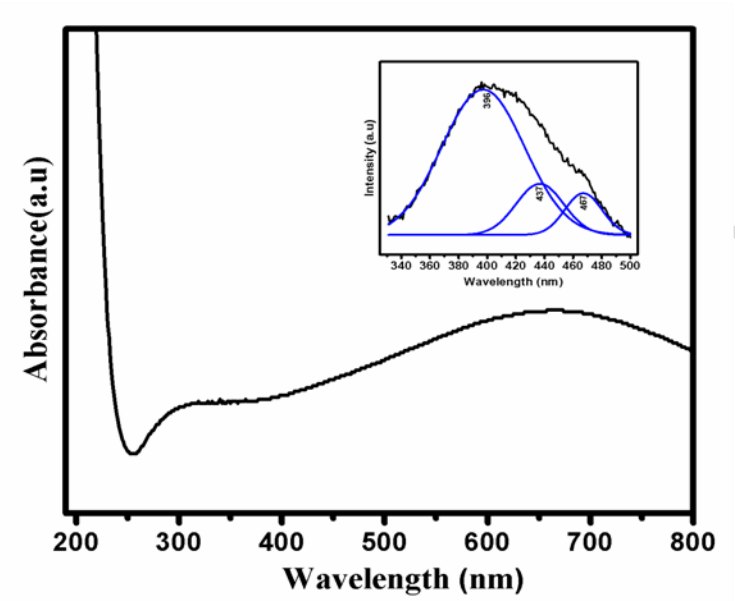

Fig. 4 UV-Vis spectrum of Te Nps (fluorescence spectrum of Te Nps with Gaussian fit in the inset).

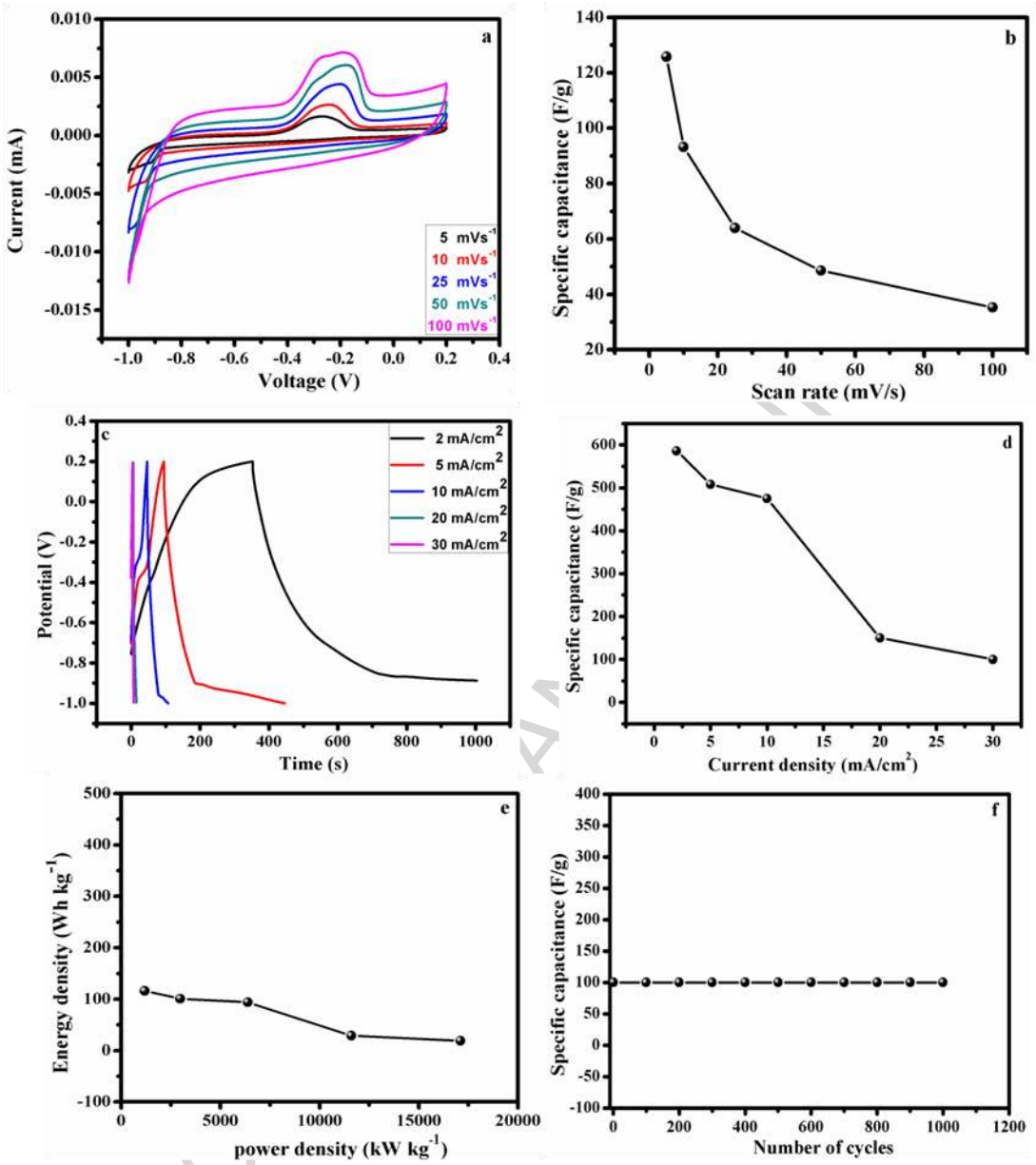

Fig. 5 (a) CV for different scan rates (b) Specific capacitance Vs scan rate plot, (c) Charge/discharge curves for different current densities, (d) Variation of specific capacitance with current density, (e) Ragone plot, (f) Cyclic stability of at 30 mA/cm^2 of Te Nps.

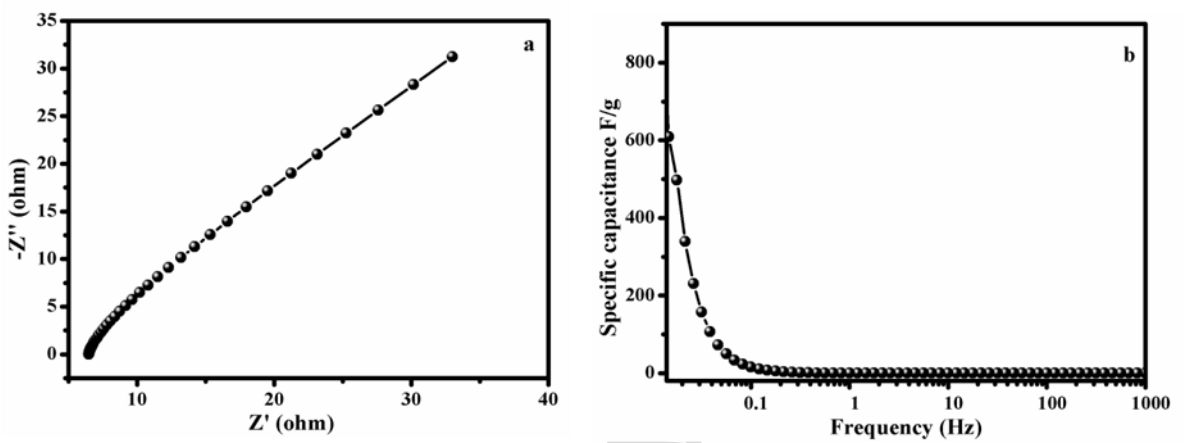

Fig. 6 (a) Impedance plot of Te Nps, (b) Frequency dependent specific capacitance of Te Nps

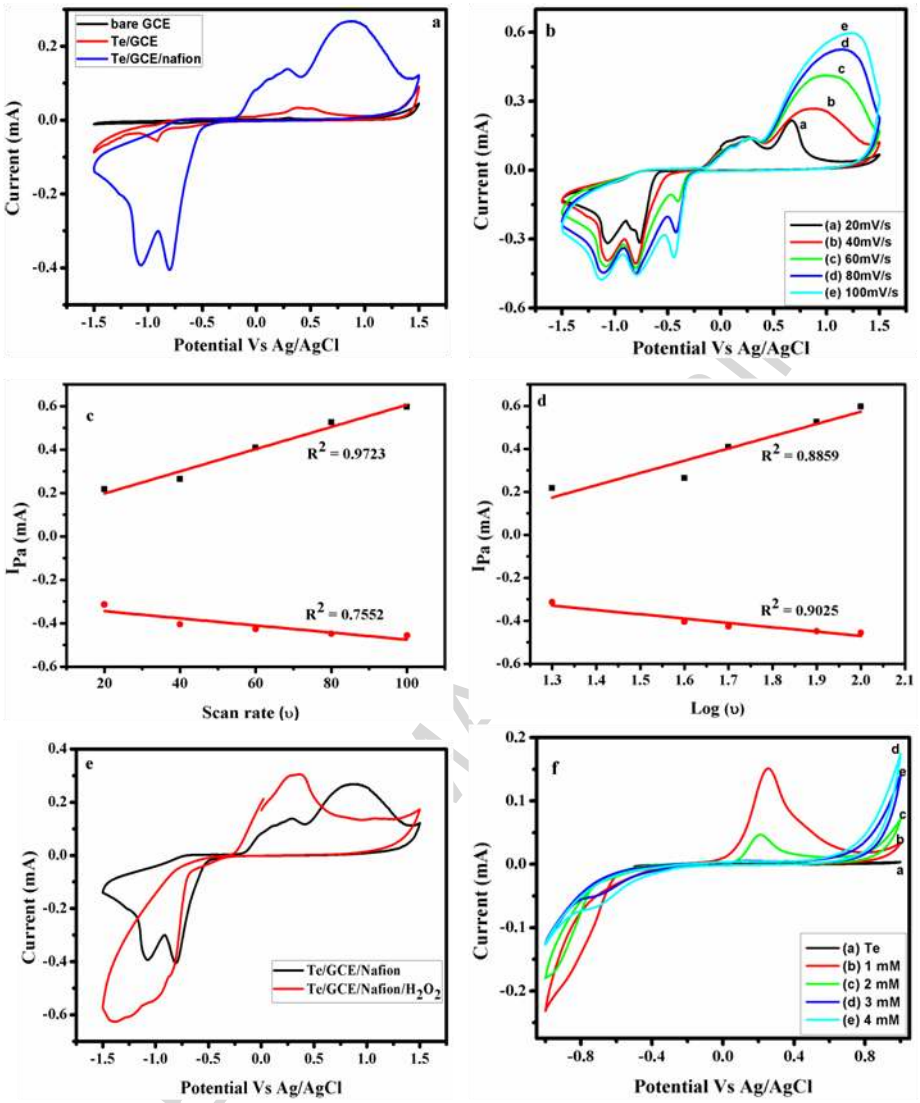

Fig. 7 (a) CV for bare GCE, GCE/Te and GCE/Te/Nafion, (b) CV of GCE/Te/Nf at different scan rates, (c) Plot for cathodic and anodic peak current against scan rate. (d) Plot for cathodic and anodic peak current against log (v), (e) CV for GCE/Te/Nf and GCE/Te/Nf, (f) CV for GCE/Te/Nf with different concentrations of H_2O_2.

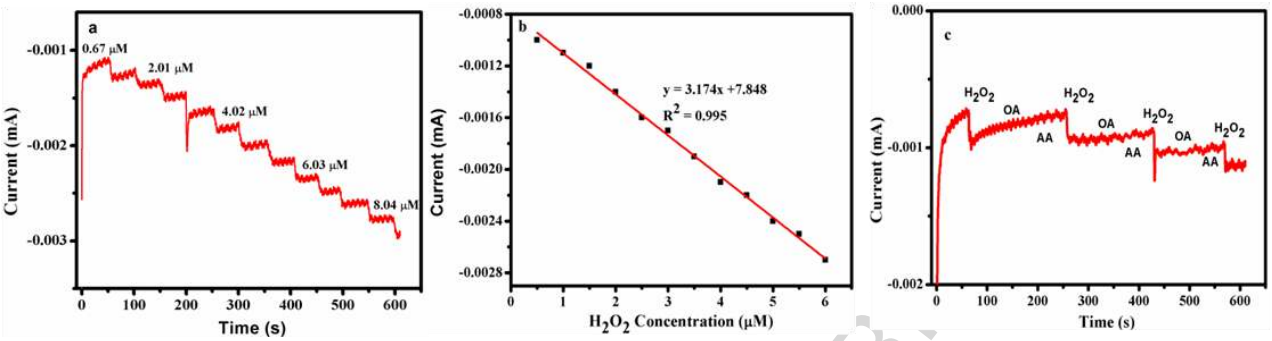

Fig. 8 (a) Chronoamperometric analysis for different concentrations of H_2O_2 (b) linear relation between current and H_2O_2 concentrations, (c) Chronoamperometric analysis with the addition of H_2O_2, OA and AA.

Highlights

- A wet chemical approach for the preparation of tellurium nanoparticles
- Excellent cycle life with 100% Coulombic efficiency
- High energy density (116 $Whkg^{-1}$) and power density (1186 Wkg^{-1})
- High sensitivity and selectivity towards H_2O_2